Contributions to Mineralogy and Petrology (2020) 175:46
https://doi.org/10.1007/s00410-020-01681-5

ORIGINAL PAPER

A mapping approach for the investigation of Ti–OH relationships in metamorphic garnet

Julien Reynes[1] · **Pierre Lanari**[1] · **Jörg Hermann**[1]

Received: 9 January 2020 / Accepted: 2 April 2020

Abstract

Garnet is a nominally anhydrous mineral that can incorporate several hundreds of ppm H_2O in the form of OH groups, where H^+ substitutes for cations in the garnet structure. To understand the effect of such small amounts of H_2O on the physical and chemical properties of garnet, it is essential to determine where and how the OH groups are incorporated into the mineral structure. We investigated correlations between major and minor element maps acquired with the electron probe microanalyser and H_2O maps measured with Fourier transform infrared spectroscopy coupled to a focal plane array detector at the microscale to determine possible coupled substitutions. A set of algorithms was developed to match the maps pixel by pixel. They allow the computation of the garnet structural formula taking the H_2O content into account and the calculation of correlations between H_2O and other elements on the basis of 10,000 s of points. This new approach was applied to two hydrous garnet samples both showing H_2O and chemical zoning. The first sample consists of a grossular-rich garnet from a high-pressure metarodingite ranging from 200 to 900 ppm H_2O. The second sample contains a Ti-rich andradite garnet ranging from 200 to 8500 ppm H_2O. For the grossular-rich garnet, a 1:1 correlation between Ti and H has been observed suggesting that H occurs as tetrahedral $(2H)^{2+}$ point defect, charge compensated by 2 Ti^{4+} on the octahedral site. Based on this, a new hydrous garnet endmember with the formula $Ca_3Ti_2H_2Si_2O_{12}$ is proposed. This $2Ti^{VI} \leftrightarrow (2H)^{IV}$ exchange mechanism is mainly responsible for the high amounts of TiO_2 (up to 11 wt%) in the investigated Ti-andradite. The incorporation of $(2H)^{2+}$ instead of $(4H)^{4+}$ on the tetrahedral site has important consequences for the normalisation of the garnet and hence on the determination of Fe^{2+}/Fe^{3+} based on stoichiometry. In the garnet from the metarodingite, a small-scale zoning in H_2O contents of less than 100 µm can be resolved, indicating that the Ti–H defect is stable up to eclogite facies conditions and not modified by diffusion even at timescales of millions of years.

Keywords Quantitative compositional mapping · Garnet · FTIR mapping · Nominally anhydrous minerals

Introduction

Garnet is a common metamorphic mineral formed during prograde dehydration reactions such as encountered during the subduction of oceanic crust and sediments. The garnet formula contains neither H_2O nor OH groups; nevertheless, it can incorporate several hundreds of ppm H_2O as OH groups where H^+ incorporation is charge-balanced by cation substitutions. Because of the large P–T stability field of garnet, the incorporated H_2O can be transported inside the slab to the deep mantle and might play an important role in the Earth's deep water cycle. It is essential to know where the OH groups are located in the garnet structure, and which coupled substitutions exist for the incorporation of H^+. The dominant substitution found so far is the replacement of a Si^{4+} cation by $4H^+$, known as the hydrogarnet point defect (Cohen-Addad et al. 1967; Foreman 1968; Lager et al. 1987). Other point defects have been proposed, involving H^+ substitutions for dodecahedral and octahedral cations (Andrut et al. 2002; Basso et al. 1984; Geiger et al. 1991). Coupled substitutions have been invoked such as H–B and H–Li point defects (Lu and Keppler 1997) and even incomplete

---

Communicated by Hans Keppler.

Electronic supplementary material The online version of this article (https://doi.org/10.1007/s00410-020-01681-5) contains supplementary material, which is available to authorized users.

✉ Julien Reynes
julien.reynes@geo.unibe.ch

[1] Institute of Geological Sciences, University of Bern, Baltzerstrasse 3, 3012 Bern, Switzerland

silicon vacancies, like $3H^+$ substituting for a Si^{4+} and being compensated by Ti^{4+} in octahedral site (Khomenko et al. 1994), or Fe^{3+} or Fe^{2+} together with one of two H^+ in the tetrahedral site in Ti-rich garnets (Kühberger et al. 1989). Recent studies support that multiple point defects are present in single garnet grains (Geiger and Rossman 2018; Reynes, et al. 2018). It has been shown that garnet composition does influence the incorporation of OH groups in the garnet structure. Garnet is a complex solid solution involving various endmembers. Spessartine (Mn–Al), almandine (Fe^{2+}–Al), pyrope (Mg–Al) constitute the widespread pyralspite subfamily, whereas grossular (Ca–Al), andradite (Ca–Fe^{3+}) and uvarovite (Ca–Cr^{3+}) belong to the ugrandite subfamily. Garnet dominated by ugrandite endmembers can incorporate up to several wt% H_2O (Rossman and Aines 1991), whereas pyralspite garnets usually incorporate only a few hundreds of ppm (Aines and Rossman 1984). Spessartine can incorporate more water (up to 1000 ppm H_2O, Arredondo et al. 2001) than pyrope and almandine (< 150 ppm H_2O). Because garnet has these various solid solutions and their affinity for H_2O seems to differ, a correlation between major elements and OH groups at a comparable scale is needed. Major and minor element chemistry of garnet is usually measured by Electron Probe Micro-Analysis (EPMA), which allows mapping with a resolution up to 1 µm. Fourier transform infrared spectroscopy (FTIR) is the optimal analytical technique to measure OH groups in garnet. This method has various advantages: (1) high resolution (down to ~ 5 µm with appropriate objective and detector); (2) low limit of detection (~ 1 ppm H_2O); (3) the wave number of absorption bands is specific to the environment where H^+ is located: the band positions vary with the nearest neighbours of the vibrating OH group and is then influenced by local charge balance; (4) it is relatively cheap and fast. Therefore, the challenge to investigate H^+ substitution in garnet is to match compositional maps obtained with these two different analytical techniques.

This study presents a novel approach and a set of programs for stacking H_2O maps acquired by FTIR with quantitative compositional maps obtained by EPMA. This allows matching pixel by pixel of the two maps, providing a database of 10,000 s to 100,000 individual points that can be statistically assessed to determine coupled substitutions involving H^+ in garnet. Advanced processing of the FTIR data using deconvolution of the spectra provides additional information of the structural position of OH groups in the garnet structure. This technique was applied to a grossular-rich garnet from a metarodingite from Servette (Aosta valley, Italy), and a Ti-rich andradite from a metapyroxenite layer in ultramafic rocks from Valmalenco (Italy). In both cases, a strong correlation between the minor element Ti and H_2O contents was found and a new hydrous garnet endmember with the formula $Ca_3Ti_2H_2Si_2O_{12}$ is proposed. The influence of H substitution on the computation of Fe^{2+}/Fe^{3+} ratios in garnet, which can be used as a redox indicator, is also assessed.

Samples and techniques

Sample description

The two samples presented in this work were collected in the Alps. The first sample *ServRod* is a garnet from a rodingite from the Servette area (St Marcel, Aosta valley, Italy). The various rock types in this area are interpreted as both oceanic and continental margin units derived from the Mesozoic Tethyan ocean and the Palaezoic crust of the African margin (Tartarotti et al. 2017). The area of St. Marcel is known for metabasalts hosting a Fe–Cu sulphide deposit and a Mn-ore deposit (Praz Borna), both related to oceanic hydrothermal processes. The mafic–ultramafic rock suite experienced extensive oceanic metasomatism, followed by high-pressure metamorphism during the Alpine subduction with peak metamorphism at 550 ± 60 °C and 2.1 ± 0.3 GPa (Martin et al. 2008). These conditions were derived from talc-schists that are associated with serpentinites. Within the same serpentinites, meta-rodingite occurs as meter-sized boudins that are interpreted to derive from mafic dykes that experienced rodingitisation during the seafloor alteration. The close link between the talc-schists, serpentinites and meta-rodingites suggests that all rock types share a common metamorphic evolution. The meta-rodingites are composed of 60% brownish garnet and 40% green diopside. Garnet grains are 1–3 mm in diameter, rock forming, automorphic with no evidence of resorption. No low-pressure hydrous mineral associated with retrogression was observed in the sample (see supplementary Figure S1 for optical image).

The second sample *TiAnd* was collected in Valmalenco, Italy. It consists of 5–10-mm-sized garnet crystals in a metapyroxenite layer identified as melanite (Ti-rich andradite). Details about this sample were previously published by Müntener and Hermann (1994). Garnet formed in equilibrium with diopside, chlorite and minor ilmenite, perovskite and magnetite and is thought to have crystallised at low pressures of 0.5 ± 0.2 GPa and a maximum temperature of 400–450 °C. The garnet grains are optically zoned, with a black melanite core surrounded by a large yellow-brownish andradite rim (see supplementary Figure S1 for optical image).

The garnets were cut near the centre of each grain. Both samples were prepared as double polished thick sections on a glass slide (280 µm for ServRod and 162 µm for TiAnd). This thickness was selected to get (1) good optical transmission and (2) a low H_2O detection limit with infrared spectroscopy. Electron microprobe X-ray mapping was performed first, before transmission infrared spectroscopy, which requires detaching the thick sections from the glass. The two techniques have different excitation volumes, as one is a near-surface analysis (EPMA) and the other a transmission technique (FTIR). This point is discussed in detail below.

Analytical techniques

Electron microprobe (EPMA)

Major elements maps of garnet were acquired using a JEOL JXA 8200 superprobe instrument at the Institute of Geological Sciences, University of Bern. Thick sections were polished to ¼ µm and carbon coated. The accelerating voltage was set to 15 keV and the beam current to 100 nA for mapping and 20 nA for conventional spot analyses. A set of spot analyses was also acquired in the mapped area for calibration. The following elements were measured: Si, Ti, Al, Cr, V, Fe, Mn, Mg and Ca and calibrated using a set of natural and synthetic standards: almandine (SiO_2, Al_2O_3, FeO); anorthite (CaO); ilmenite (TiO_2); tephroite (MnO); olivine (MgO); spinel (Cr_2O_3); shcherbinaite (V_2O_3). Peak and background were measured for 20 s and 2 × 10 s, respectively for spot analyses and a dwell time of 150 ms was used for mapping. Two maps were acquired: a map of 1000 × 1000 pixels with a step size of 2 µm on the ServRod sample and a map of 650 × 650 pixels with a step size of 8 µm for TiAnd. The maps were calibrated and further analysed using XMapTools 3.2.1 (Lanari et al. 2014, 2019). No time-related intensity drift was observed using the monitoring tools available in XMapTools (see discussion and examples in Lanari et al. (2019)).

Fourier transform infrared spectroscopy (FTIR)

FTIR utilises vibration of OH groups when exposed to specific wavelengths of radiation. A specific region of the mid-infrared, approximately 3000–3800 cm^{-1}, typically corresponds to the stretching frequency of OH groups in silicates. Measured absorbance enables quantification of the OH content in the sample. This content is determined using the Beer–Lambert law with specific absorption coefficients and is commonly expressed as H_2O ppm by weight (µg/g). FTIR also provides information on the structural environment of these OH groups.

Transmission FTIR spectroscopy maps were acquired at the University of Bern. The instrument is equipped with a Plexiglas chamber with controlled airflow and moisture to limit environmental variations of CO_2 and H_2O (relative humidity < 10%). This instrument has two detectors: a single spot, nitrogen-cooled mercury cadmium telluride (MCT) detector and a focal plane array (FPA) detector—composed of 64 × 64 = 4096 liquid nitrogen-cooled MCT elements on a square array. The minimum pixel size is 2.7 µm × 2.7 µm. A 2 × 2 to 8 × 8 binning was used blowing up the pixel size to, respectively, 5.4 × 5.4 µm and 21.6 × 21.6 µm, but improving the quality of each spectrum. The choice of binning was also motivated by the size of the area measured, as the Bruker® OPUS® program cannot acquire maps containing more than 200,000 spectra. Garnet from Servette Rodingite was measured with a binning by 2 of the FPA detector and a pixel size of 5.4 µm. The map represents 14 × 14 tiles of 172.8 µm with 1024 spectra per tile—leading to 200.704 spectra in total. 140 scans per spectrum were chosen to complete the map in less than 5 h—the maximum autonomy of cooling of the FPA detector. For the second sample TiAnd, a map of 35 × 35 tiles and a binning of 8 was set—leading to a pixel size of 21.6 µm—78.400 spectra, and 10 scans per spectrum. The relatively low number of scans was required to maintain the measurement time below 5 h. The data quality is still good as the binning of the detector improves the signal to noise ratio. Each spectrum was acquired in the middle infrared between 900 and 4000 cm^{-1} with 8 cm^{-1} wavenumber resolution. Spectra were baseline corrected using the concave rubber band algorithm of OPUS® with 64 points and four iterations. For TiAnd, pseudo-transmission measurements were acquired using an ATR objective coupled with the single-spot MCT detector. The objective is composed of a germanium crystal touching the sample, resulting in an evanescent wave of infrared light that is transmitted through the uppermost portion of the sample, allowing measurement of a very thin layer at the surface of the sample, with a penetration of less than 1 µm and a spot size around 30 µm (see supplementary material S2 for details). This method allows high water contents, up to several wt% H_2O to be measured but it does not detect low water content < 1000 ppm H_2O because of the small penetration depth.

Data processing

OPUS and *FPAMap*

OPUS®, the main Bruker® FTIR program, was used for data visualisation, baseline subtraction and, where needed, atmospheric H_2O compensation. An in-house program *FPAMap* was developed as a MATLAB®-based graphical user interface (GUI) for advanced data processing. It reads the integrated areas determined by OPUS from the OH stretching region and overtone. In the case of garnet, the OH stretching region results in absorbance at 3400–3800 cm^{-1} and the overtone region—associated with harmonics of Si–O bonds vibrations—produces absorption bands at 1600–2000 cm^{-1}. For the sample ServRod, an overtone–thickness relationship was applied to correct for small variations in the thickness of the sample (thickness = 1.2786 × overtone, see Reynes et al.

(2018)). The absorption map for water is then normalised to 1 cm thickness of garnet. The H_2O content (in µg/g H_2O) is computed, using an appropriate absorption coefficient k_{abs} defined by the following equation:

$$k_{\mathrm{abs}} = \frac{c \times M_{\mathrm{H_2O}}}{d \times \varepsilon}, \quad (1)$$

where c is a normalisation constant equal to 10^6 (corresponding to the conversion from g/g to µg/g (ppm H_2O), $M_{\mathrm{H_2O}}$ is the molar mass of H_2O, d is the density of the mineral and ε the extinction coefficient, a.k.a calibration coefficient—determined by an independent method and specific to a mineral. The coefficient from Maldener et al. (2003) for grossular, $\varepsilon = 14{,}400\ \mathrm{l{\cdot}mol^{-1}{\cdot}cm^{-2}}$ was chosen, where a H_2O content of 870 ppm was derived by nuclear reaction analysis (NRA) on a grossular crystal. A complementary study by Reynes et al. (2018) has shown that this coefficient is suitable for grossular-rich garnet.

In the case of the TiAnd sample, a thickness correction based on overtone was not possible because of compositional variability affecting the overtone region shape and absorption and thus a constant thickness of 162 µm, measured with a Mitutoyo® micrometer, was used. The overtone map was only used to detect mineral inclusions. The same extinction coefficient ε was used (see below for justification). The output file of *FPAMap* contains a H_2O content map of the sample, expressed in ppm H_2O.

StackMaps

A second GUI-based program, *StackMaps*, was designed for the superposition of FTIR and EPMA maps. As the two datasets were obtained on two different instruments, and the sections were detached from the glass to be measured by transmission on FTIR, it was impossible to analyse the same area with the same resolution and orientation. The FTIR map was acquired on a larger zone, and a geometric transformation based on a set of reference points (crystal edges, cracks, inclusions) is needed to find the correct position relative to the EPMA maps via affine transformation, combining translation, scaling, shearing and rotation. As the pixel size is different, the map with the lowest resolution (FTIR) was resampled based on the highest resolution (EPMA). The output of *StackMaps* is a H_2O map with the same orientation and resolution than the EPMA map. The major element composition of each pixel is known as well as the corresponding H_2O content allowing a structural formula to be calculated. This correction is required as the FTIR map can be distorted, due to lower accuracy of the stage and binning, in comparison to microprobe map.

This program has been incorporated as an add-on in the mapping package XMapTools (Lanari et al. 2014, 2019).

GarnetH$_2$O

The third program *GarnetH$_2$O* is an external function of XMapTools for generating maps of structural formula of garnet based on the maps of SiO_2, TiO_2, Al_2O_3, Cr_2O_3, V_2O_3, FeO, MnO, MgO, CaO and H_2O expressed in mass weight percentage of oxide. Normalisation is done on a basis of eight cations, with the possibility of counting $(2H)^{2+}$ or $(4H)^{4+}$ as one cation, as they do substitute for one silicon. For this study, there is good evidence that H is incorporated in the garnet as $(2H)^{2+}$. Therefore, garnet normalisation assumes all H as $(2H)^{2+}$ and a fixed cation number of 8. The proportion of Fe^{2+} and Fe^{3+} is then adjusted assuming a sum of charges of 24 (see supplementary material S3). The tetrahedral site is considered as being occupied by Si^{4+}, Hx ($(2H)^{2+}$ or $(4H)^{4+}$) and potentially Al^{3+}, octahedral site by Ti^{4+}, Al^{3+}, V^{3+}, Cr^{3+}, Fe^{3+} and in the case of Ti-rich andradite garnets Fe^{2+} and Mg^{2+} and Mn^{2+}. The dodecahedral site has Ca^{2+}, Mn^{2+}, Mg^{2+} and Fe^{2+}, only Ca^{2+} and Mn^{2+} for Ti-rich andradite.

Deconvolution and correction of artefacts

A deconvolution was applied to the spectra of both maps to better resolve the water region and define the relative contributions of each peak. The code, written in MATLAB®, uses a modified version of the *peakfit* function developed by Tom O'Haver (2015). The position of the different peaks is fixed, and the program only adjusts the peak heights and widths to fit the measured signal. Results consist of height, width and area data for each peak, which can be displayed as maps as well. The same resampling algorithm and geometric transformations were applied as previously described for the FTIR water map.

For the sample ServRod, fluid inclusions caused a broad absorption band centred at 3420 cm^{-1}. A specific algorithm was used to model fluid inclusion by fitting this region with a broad Gaussian centred on 3420 cm^{-1}—and minimising the residual area between 3400 and 3100 cm^{-1}. This procedure was applied to each spectrum and resulted in a map of fluid inclusion density. The spectra were corrected for fluid inclusion. Only the garnet OH stretching group bands are discussed in the following.

Results

EPMA maps

Compositional maps obtained by EPMA are presented in Fig. 1 for ServRod and Fig. 2 for TiAnd (additional

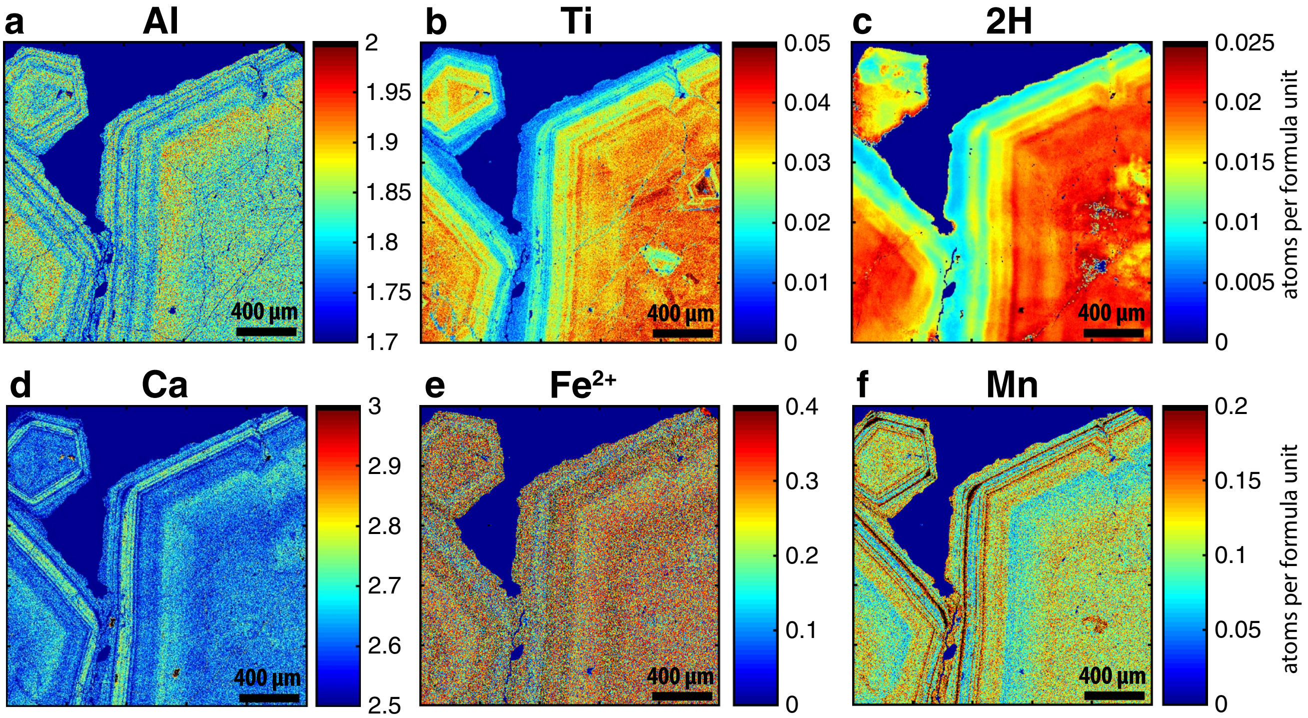

Fig. 1 Element maps acquired by EMPA for sample ServRod. Each map is expressed in atoms per formula units (apfu). Normalisation was done using 24 charges, 8 cations and $(2H)^{2+}$ counting as a cation

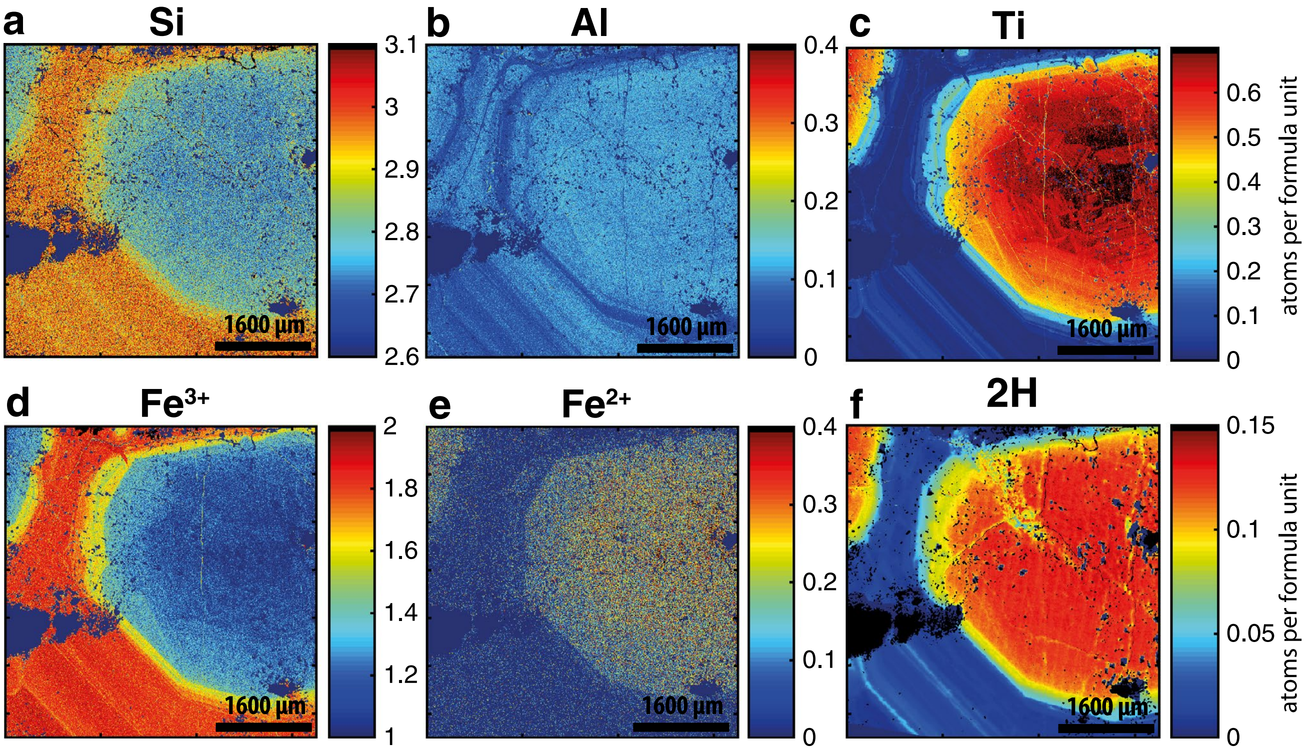

Fig. 2 Element maps acquired by EMPA for sample TiAnd. Each map is expressed in atoms per formula units (apfu). Normalisation was done using 24 charges, 8 cations and $(2H)^{2+}$ counting as a cation

compositional maps are presented in supplementary material S4). These maps are expressed in atoms per formula units (apfu), calculated on an eight cations basis.

ServRod garnet shows a high Ca (> 2.6 apfu) and Al content (> 1.7 apfu). Therefore, it is a grossular garnet with minor andradite and almandine component (see Table 1 for endmember formula). Various oscillatory zonings in dodecahedral cations such as Ca^{2+}, Fe^{2+} and Mn^{2+} as well as octahedral cations Al^{3+}, Ti^{4+} and Fe^{3+} create complex but sharp zoning patterns. The Ti content increases from the rim to core by a factor of five, varying from 0.01 to 0.05 apfu.

TiAnd garnet is mainly characterised by three chemical zones, delimited by their Ti content (Fig. 2). The rim zone, with Ti < 0.2 apfu shows a high $Fe^{3+} = 2$ apfu and a $Si^{4+} = 3$ and dodecahedral site fully occupied by Ca^{2+}—characteristic of andradite garnet. Small and sharp bands appear in the Ti map, with Ti rising from 0.1 to 0.25 apfu. The second zone is only 200 µm wide and consists of a sharp increase of Ti form 0.2 to 0.4 apfu. The core zone is characterised by a high Ti content up to 0.7 apfu and a Si deficiency (2.7 < Si < 3). The Mg content is increasing from rim (0.02) to core (0.08 apfu). The Ca pattern does not vary with the zones with a value around 3 apfu and thus Fe^{2+} and Mg^{2+} occupy octahedral sites. As a consequence, zoning involves only variations in octahedral and silicon site occupancies.

Table 1 Garnet endmembers

Dry endmembers	
$Ca_3Al^{3+}{}_2[Si_3]O_{12}$	Grossular
$Ca_3Fe^{3+}{}_2[Si_3]O_{12}$	Andradite
$Ca_3Fe^{2+}Ti^{4+}[Si_3]O_{12}$	Morimotoite
$Ca_3Fe^{3+}Ti^{4+}[Fe^{3+}Si_2]O_{12}$	Schorlomite
$Ca_3Fe^{3+}Ti^{4+}[Al^{3+}Si_2]O_{12}$	*Al–Ti Andradite*
Hydrous endmembers	
$Ca_3Al^{3+}{}_2[H_4Si_2]O_{12}$	Hydrogrossular
$Ca_3Fe^{3+}{}_2[H_4Si_2]O_{12}$	Hydroandradite
$Ca_3Ti^{4+}{}_2[H_2Si_2]O_{12}$	*Ti–hydrogarnet*

FTIR single spectra

Core to rim spectra were extracted for both samples and are shown in Fig. 3. Servette rodingite spectra (ServRod, see Fig. 3a) display three bands at 3500–3700 cm^{-1}. A main band, around 3595 cm^{-1} is flanked by two smaller bands on either side at around 3546 cm^{-1} and 3652 cm^{-1} of similar intensity. These bands are visible in all analyses from core to rim. According to peak positions and shapes, this sample is similar to class 5 grossular according to the classification of Rossman and Aines (1991) (rodingite, Liguria), despite the singularity that the main band is at lower wave number than in the classification (3595 cm^{-1} for 3612 cm^{-1}). The spectra in the core region are affected by a large bump due to fluid inclusion, centred on 3420 cm^{-1}. The overtone region, 1600–2000 cm^{-1}, shows the characteristic peak and shoulder of garnet, and allows the sample thickness to be determined (see above).

Titanium andradite (TiAnd) spectra show absorption in the range 3500–3700 cm^{-1} (Fig. 3b) similar to the Servette rodingite. Spectra corresponding to the rim zone, optically yellow-brownish, display two well-defined bands at 3563 and 3604 cm^{-1}, characteristic of pure andradite (Amthauer and Rossman 1998). Darker zones show a stronger absorption of the first band, around 3563 cm^{-1} and the appearance of a second band, around 3581 cm^{-1}, which forms a doublet with the previous. The core of the sample completely absorbs IR radiation between 3530 and 3640 cm^{-1} due to the

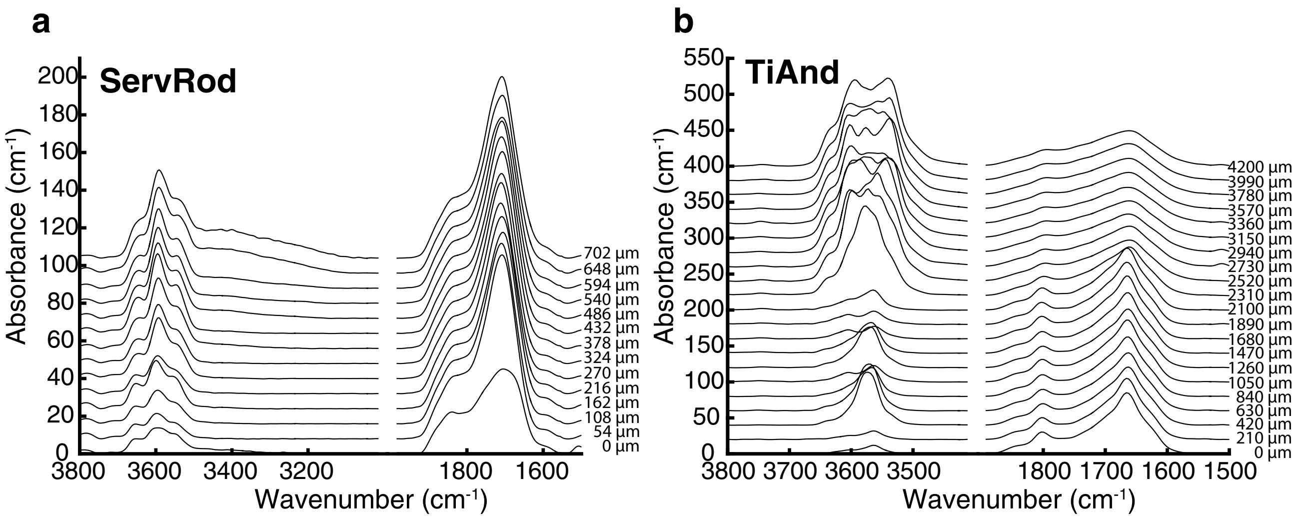

Fig. 3 Core to rim FTIR spectra in the middle infrared in region 1500–2000 cm^{-1} and 3100–3800 cm^{-1}. **a** ServRod sample, **b** TiAnd sample

high water content (> 5000 ppm H_2O). The overtone region 1600–2000 cm^{-1} shows variability between the rim characterized by sharp bands and the core zone with smoother peaks. The absorbance of these bands is modified up to 50%, though the thickness is not varying by more than 5%. These differences imply that a linear overtone to thickness law is not appropriated for this sample.

FTIR maps

The H_2O distribution maps of the two garnets (Fig. 4a, c) display surprisingly sharp, regular zoning patterns. The comparison of the H_2O zoning with the major and minor element zoning (Figs. 1, 2) provides further evidence for a strong correlation between Ti and H_2O. The map correlation algorithm *StackMaps* was used to superimpose H_2O with EPMA maps. Figure 4 shows for each sample the maps of H_2O and TiO_2 with the corrected resolution and orientation. ServRod maps (Fig. 4a, b) show oscillatory zoning in TiO_2 and H_2O. The H_2O content is increasing from 300 ppm H_2O at the edge of the crystal to 900 ppm H_2O in the interior, while TiO_2 increases in a similar pattern from 0.2 to 0.9 wt%. The noisy zone present on the top left corner of the water map is an artefact linked to the smaller size of the analysed grain. TiAnd (Fig. 4c, d.) reveals one order of magnitude higher TiO_2, from the rim below 1 wt% up to 10 wt% in the core. Similarly, the H_2O content ranges from 300 to 5000 ppm inward. As shown in Fig. 3, the H_2O content in the core of the sample is underestimated due to the nearly complete absorption of the infrared light.

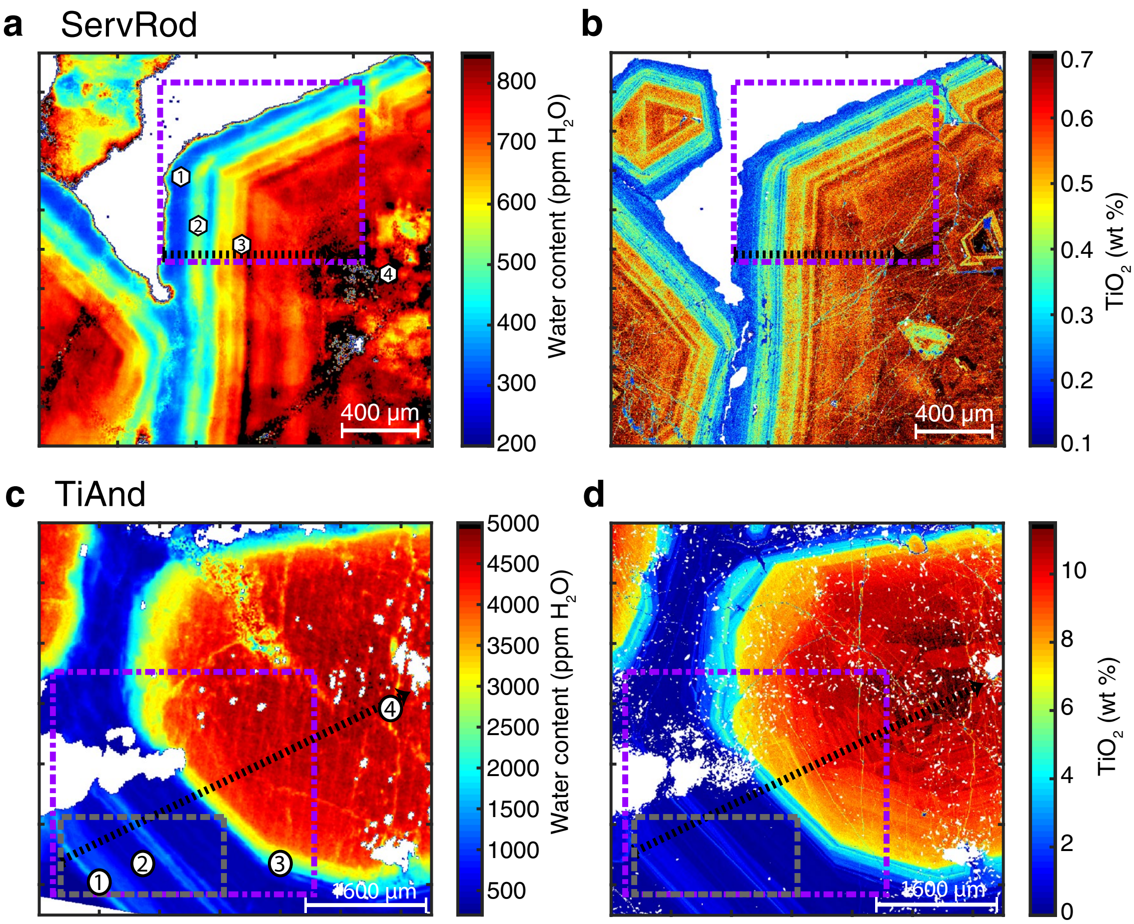

Fig. 4 H_2O content map obtained from FTIR measurements (**a**, **c**) and compositional map of TiO_2 content in wt% (**b**, **d**) for sample ServRod and TiAnd, respectively. The dashed black lines represent the positions of the profiles which are displayed in Fig. 3 and for TiAnd the profiles in Fig. 5. Grey dashed rectangular area on subfigure **c** corresponds to the area used for map deconvolution presented in Fig. 10. Purple dashed line rectangular shape is delimiting the part used for detailed analysis in Fig. 6a–e for ServRod and Fig. 6b–f for TiAnd. Deconvoluted spectra of spots 1–4 for ServRod are displayed in Fig. 7 and spots 1–4 for TiAnd are displayed in Fig. 8. White zones on maps are inclusions, artefacts and zones corresponding to another phase than the mineral of interest

ATR profile

To deal with complete absorption issues in the core of TiAnd, a rim–core profile was measured on the same grain with the ATR objective, using a spectral resolution of 8 cm^{-1}, 512 scans and a step size of 45 µm. The profile is presented in Fig. 5, and is located in Fig. 4—it follows the FPA profile presented in Fig. 3b. In Fig. 5a, the integrated absorption between 3400 and 3700 cm^{-1} is displayed together with the integrated absorption measured with the FPA detector. Distinct features noticed on the two profiles (purple dots) enable to calibrate the ATR spectra for H_2O content and compute the effective penetration depth of the IR beam in the range 3500–3700 cm^{-1} which is 0.56 µm (details in supplementary material S5). While the FPA profile reaches complete absorption and a flat trend of H_2O content towards the core at about 5000 ppm H_2O, the ATR profile reveals a higher content up to 8000 ppm H_2O. Using the ATR profile (Fig. 5), an average H_2O content of 6100 ppm in the core can be recalculated, assuming a spheric approximation of the garnet. This is in excellent agreement with the 6600 ± 1000 ppm H_2O obtained for separated garnet cores measured for the bulk water content by thermal combustion measurements (Müntener and Hermann 1994). This underlines that the coefficient chosen for calibration of the IR spectra, 14,400 $l\cdot mol^{-1}\cdot cm^{-2}$ (Maldener et al. 2003) for a grossular garnet is also appropriate for Ti-rich andradite. Detection limits appear to be in the region of 500 ppm H_2O, which is impressive considering that the depth of penetration is below 1 µm with the ATR objective.

Correlation maps and correlation plots

For both samples, H_2O and TiO_2 contents are increasing from rim to core (Fig. 4). To test coupled substitutions, the molar abundance is required to quantify by how many moles H increases with one mole of Ti.

The notation $n^* x$ corresponds to the number of moles of x within one tonne of mineral.

$n \times$ H is computed using

$$n^*\mathrm{H} = \mathrm{H_2O(ppm)} \times \frac{2}{M_{\mathrm{H_2O}}} \tag{2}$$

with H_2O in ppm and M_{H2O} the molar mass of H_2O (18.015 $g\cdot mol^{-1}$). Similarly, $n \times$ Ti is obtained using

$$n^*\mathrm{Ti} = \mathrm{TiO_2(wt\%)} \times \frac{1}{M_{\mathrm{TiO_2}}} \times 10,000 \tag{3}$$

with TiO_2 wt% and M_{TiO2} the molar mass of TiO_2 (79.866 $g\cdot mol^{-1}$). Two rectangular areas free of artefacts and representative of the variations were selected for further investigation. The results are presented in Fig. 6 containing 100,000 pixels for the ServRod and 110,000 pixels for the TiAnd maps. The value of n^* Ti for each pixel was plotted in a binary diagram against the corresponding n^* H for both samples and the results presented as density maps (Fig. 6c, d). Each pixel colour is proportional to the number of analyses (i.e. originally pixels of the maps shown in Fig. 6a, b) overlapping the pixel using a logarithmic scale. For ServRod, the yellow zones on density maps correspond to density above 50 analyses, and represent the main compositional

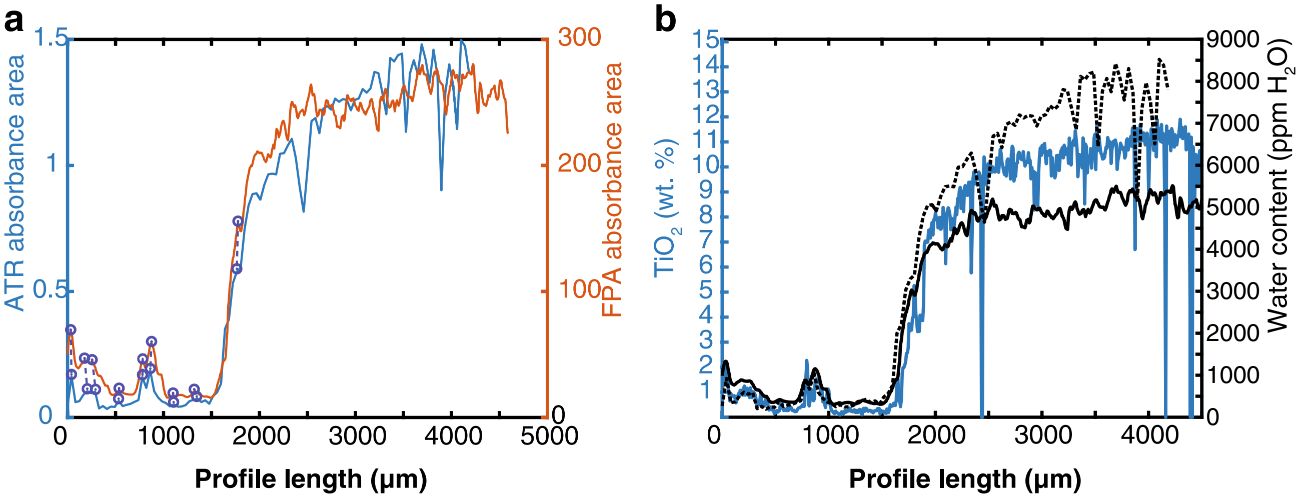

Fig. 5 Multiple profiles acquired by FTIR and microprobe along the same line. **a** Integrated ATR (< 1 µm penetration) absorbance (blue) and FPA transmission measurement absorbance (red) along the same profile drawn in Fig. 4c–d. Purple dots are the reference points used to calibrate the penetration depth of the IR light using the ATR objective. **b** H_2O content profile (in ppm) computed from FTIR-FPA measurements (in black straight line), water-content profile computed from FTIR-ATR measurements (in black dashed line) and TiO_2 wt% profile (in blue)

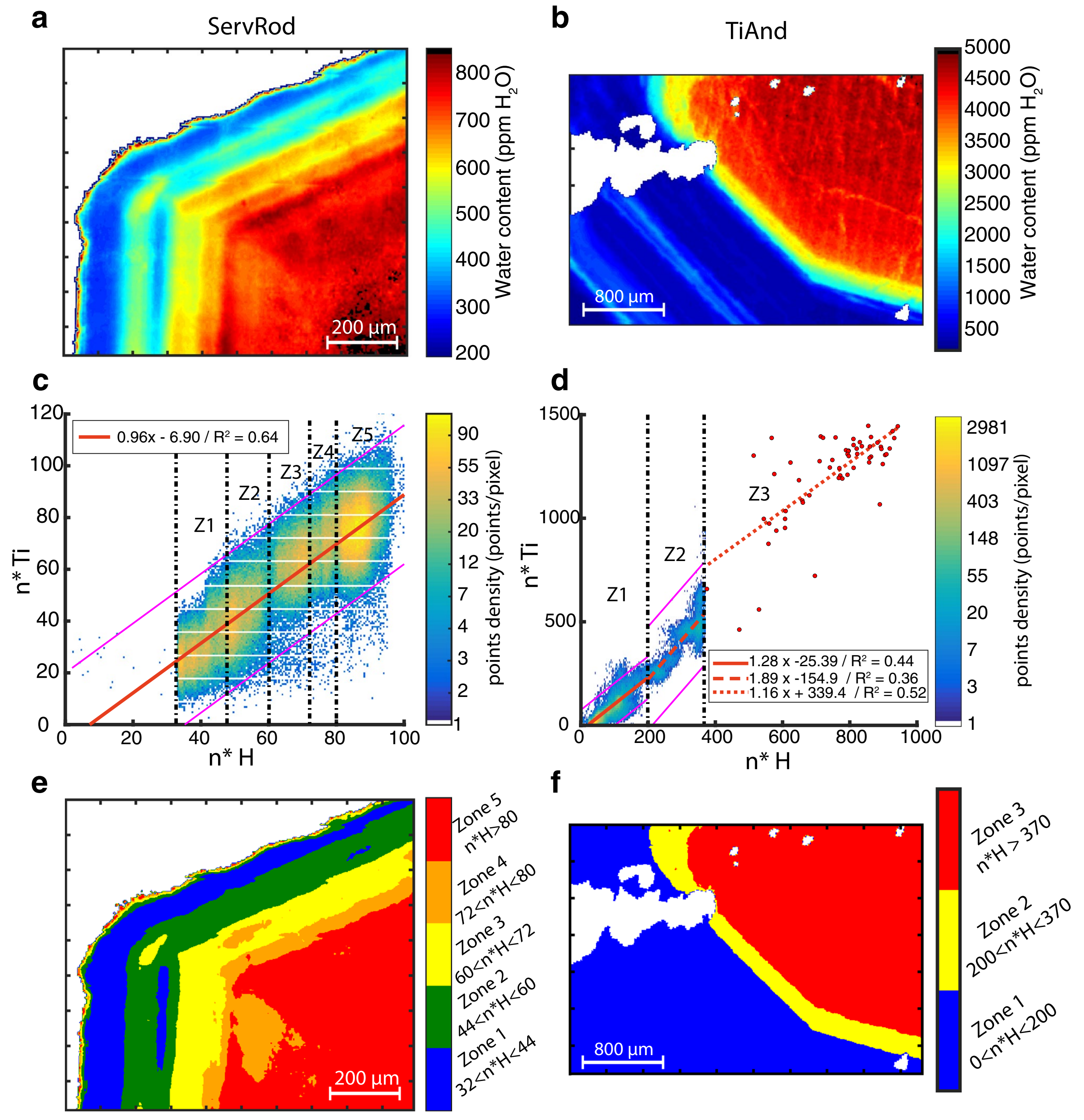

Fig. 6 Selected parts of the water maps (see Fig. 4 for location) for detailed analysis (**a**, **b**). White zones represent other phases than garnet. **c**, **d** Density plot showing n^* H versus n^* Ti in mol·t^{-1} (see text for meaning of these notations). Each point takes a colour value, which is determined by the number of points overlapping the marker. Regression lines in red are shown together with coefficient of determination (R^2). Vertical dashed lines are delimitations of different zones identified on maps (**e**) and (**f**)

groups in the crystal. This dataset was classified into five compositional groups (Fig. 6e). The linear fit between Ti and H has a slope of 0.96 over all five zones (Fig. 6c). In the case of the TiAnd sample (Fig. 6d), the relationship between n^* Ti and n^* H was investigated separately in three regions of compositions (Fig. 6f) corresponding to (1) the low-Ti rim, (2) the intermediate mantle and (3) the core enriched in Ti. For n^* H ranging between 0 and 200 mol·t^{-1}, the linear regression has a slope of 1.28. The slope changes to 1.89 for the region with n^* H comprised between 200 and 370 mol·t^{-1}. Over 370 mol·t^{-1}, water measurement by transmission is not reliable because of nearly complete absorption. Therefore, for n^{*} H > 370 mol·t^{-1}, only single points extracted from the ATR profile presented in Fig. 5 are plotted, and the regression gives a slope of 1.16.

Structural formula and substitution mechanism

The full quantification of garnet composition involving also water provides the basis for the calculation of the structural formula. Selected EPMA data of ServRod are presented in Table 2 and TiAnd on Table 3. In ServRod, there is a slight decrease of Si (in apfu) from rim to the core with a concomitant increase in 2H. Only in the core, a small amount of Al is required to fill the tetrahedral site. The excellent correlation of H to Ti (Fig. 6c) is also noted in the structural formula with twice as much Ti than 2H. This suggests that the coupled substitution of 2H on the Si site is charge balanced by 2Ti on the octahedral site. There is not enough Al and Ti to fully occupy the octahedral site and thus a small amount of Fe^{3+} is required. The dodecahedral site is dominantly filled with Ca with minor Fe^{2+}, and Mn and traces of Mg.

Table 2 Selected microprobe analysis of ServRod sample

ServRod	Point1	Point2	Point3	Point4
SiO_2	39.65	39.29	38.65	38.69
Al_2O_3	20.38	20.30	20.20	20.46
Cr_2O_3	bdl	bdl	bdl	bdl
TiO_2	0.15	0.33	0.62	0.77
FeO_{total}	6.49	4.69	4.77	5.91
FeO	3.85	2.03	2.73	3.85
Fe_2O_3	2.94	2.96	2.27	2.30
MnO	2.89	0.87	1.59	0.72
MgO	bdl	bdl	0.18	0.37
CaO	31.38	34.61	32.69	32.54
H_2O	0.03	0.05	0.07	0.09
Total	101.23	100.47	99.02	99.83
Si	3.010	2.983	2.979	2.958
2H	0.008	0.013	0.018	0.022
Al^{Tetra}	0.000	0.004	0.003	0.020
Σ Tetra	3.018	3.000	3.000	3.000
Al	1.823	1.812	1.832	1.824
Ti	0.009	0.019	0.036	0.044
Fe^{3+}	0.168	0.169	0.132	0.132
Σ Oct	2.000	2.000	2.000	2.000
Fe^{2+}	0.244	0.129	0.176	0.246
Mn	0.186	0.056	0.104	0.047
Mg	0.000	0.000	0.021	0.042
Ca	2.552	2.815	2.700	2.665
Σ Dod	2.982	3.000	3.000	3.000
Σ Charges	24.03	23.99	24.00	23.98
Σ Cations	8.000	8.000	8.000	8.000

bdl below detection limit

Table 3 Selected microprobe analysis of TiAnd sample

TiAnd	Point 1	Point 2	Point 3	Point 4	Point 5
SiO_2	35.22	35.70	34.25	34.07	32.85
Al_2O_3	0.85	0.87	0.98	1.05	1.13
Cr_2O_3	0.47	0.42	0.16	0.29	0.22
TiO_2	0.82	2.05	4.85	7.67	11.24
FeO_{total}	26.31	25.02	22.59	20.86	17.80
FeO	0.11	0.52	0.29	1.36	2.05
Fe_2O_3	29.12	27.23	24.78	21.67	17.50
MnO	0.00	0.00	0.47	0.19	0.32
MgO	0.02	0.64	0.27	0.28	0.51
CaO	33.05	32.95	33.25	33.78	33.28
H_2O	0.06	0.13	0.34	0.55	0.84
Total	99.24	100.51	99.65	100.90	99.94
Si	2.983	2.979	2.869	2.814	2.707
2H	0.017	0.037	0.094	0.151	0.231
Al^{tetra}	0.000	0.000	0.037	0.035	0.062
Σ Tetra	3.001	3.015	3.000	3.000	2.999
Al^{Oct}	0.080	0.086	0.060	0.065	0.048
Ti	0.052	0.129	0.305	0.472	0.702
Fe^{3+}	1.842	1.699	1.555	1.329	1.074
Fe^{2+}	0.016	0.047	0.027	0.108	0.149
$MgMn^{Oct}$	0.003	0.040	0.052	0.025	0.027
Σ Oct	1.993	2.000	1.999	1.999	2.000
Mg^{Dod}	0.000	0.040	0.000	0.005	0.033
Mn	bdl	bdl	0.016	0.010	0.020
Ca	2.999	2.945	2.984	2.985	2.947
Σ Dod	2.999	2.985	3.000	3.000	3.000
Σ Charges	23.980	24.000	24.000	24.000	24.000
Σ Cations	7.993	8.000	8.000	7.999	8.000

bdl below detection limit

TiAnd has the dodecahedral site filled almost completely by Ca^{2+}. Thus, Fe^{2+} and Mg^{2+} substitute into the octahedral site in the core of the garnet, providing evidence for the Morimotoite substitution occurring in Ti-rich andradite garnet $2Fe^{3+} \leftrightarrow Ti^{4+} + Fe^{2+}$ (see Table 1 for endmember definition). The core is Si deficient with 0.3–0.4 apfu missing, compensated mainly by $(2H)^{2+}$ giving raise to the coupled substitution $2Fe^{3+} + Si^{4+} \leftrightarrow 2Ti^{4+} + (2H)^{2+}$. This substitution is responsible for 2/3 of the Ti incorporation in the andradite. Some minor tetrahedral X^{3+} cations (X = Fe or Al) are needed in the high Ti-andradite following another Ti substitution mechanism^{3+}, called schorlomite $X^{3+} + Si^{4+} \leftrightarrow Ti^{4+} + X^{3+}$. Results of structural formula computation from X-ray chemical map and FTIR water maps are presented in Fig. 1 for ServRod and Fig. 2 for TiAnd, and take into account the H_2O content measured by FTIR, with H counting has $(2H)^{2+}$ cation occupying the silicon site. For ServRod sample (Fig. 1) the (2H) apfu map is equivalent to 1/2 times the Ti apfu map.

Deconvolution of spectra

The integrated absorbance permits calculation of total H_2O in the garnet structure but it does not take into account that several peaks/bands may exist for a sample, and that their positions and relative intensities may vary. However, FTIR spectra also contain detailed information regarding the environment of the OH groups in the garnet structure that can be extracted using spectrum deconvolution. The deconvolution consisted in fitting each measured spectrum with Lorentzian or Gaussian peaks to resolve the different band contribution. Four parameters were obtained for each peak: position, width (half-width—the width of the distribution at height divided by two), height and area. Selected spectra were extracted from the maps and are presented in Fig. 7 for ServRod and Fig. 8 for TiAnd. Gaussian peaks were used for the sample ServRod and Lorentzian peaks for TiAnd to obtain the best deconvolution possible for each case. Four representative spectra (see Fig. 4a for location) were selected for ServRod, and are plotted in Fig. 7. Spectra can be resolved by at least three peaks, after a correction of the signal to remove a broad Gaussian peak centred at 3420 cm^{-1} caused by fluid inclusions. The first peak around 3547 cm^{-1} does not show a strong protuberance and is most of the time limited to a shoulder, due to its proximity with the main peak. It always appears as the second peak in term of intensity and

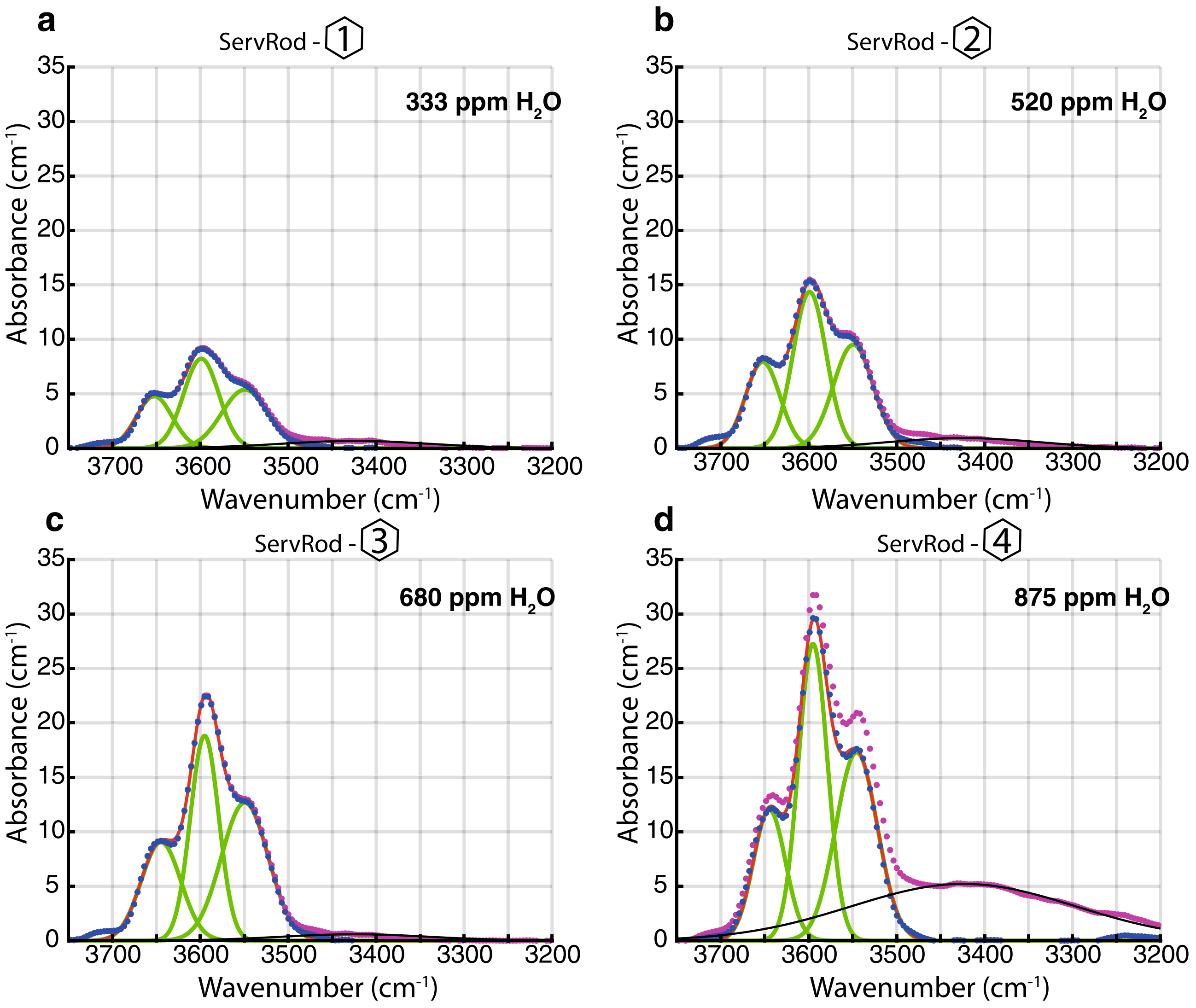

Fig. 7 Selected spectra of ServRod with associated deconvolutions. Only the OH stretching region between 3200 and 3750 cm^{-1} is displayed. The spectra positions are shown in Fig. 2a. **a** Rim spectrum, **b**, **c** mantle spectra and **d** core spectrum. All spectra are normalised to the thickness of the sample. Purple round markers are measured signal, blue round markers are the corrected signal by subtraction of fluid inclusions. The fluid inclusion corresponds to a wide Gaussian peak in black, whereas the three peaks of the deconvolution are narrow Gaussians shown in green. The sum of the three Gaussians bands is shown in red

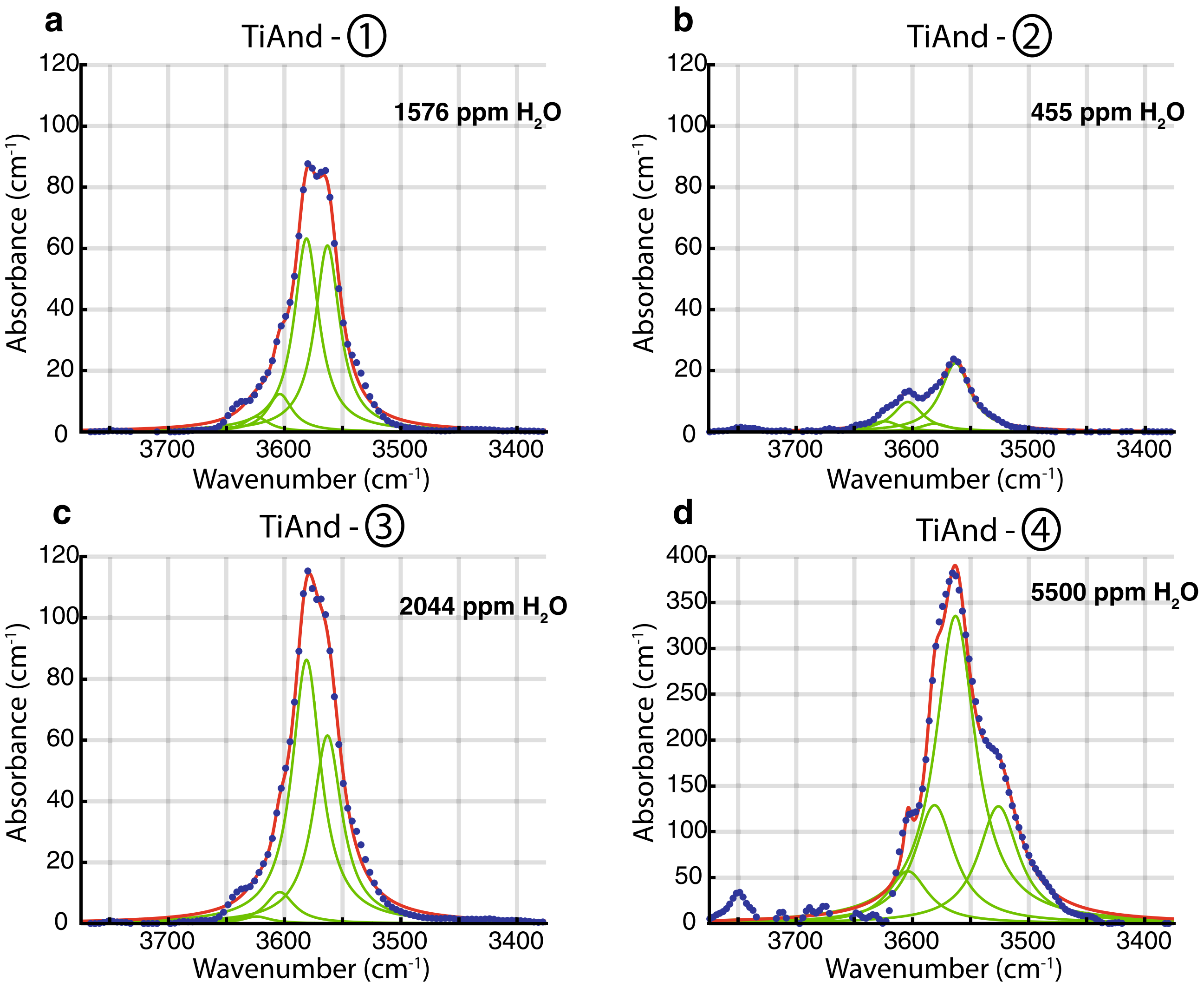

Fig. 8 Selected spectra of TiAnd sample with associated deconvolutions. Only the OH stretching region between 3400 and 3750 cm^{-1} is displayed. The spectra positions are shown in Fig. 2c. **a** Ti-enriched zone in the rim acquired with ×15 objective, **b** low-Ti zone acquired with ×15 objective, **c** start of the high-Ti zone towards the core acquired with ×15 objective and **d** core spectra acquired with ATR objective. The measured data are shown with blue dots, in green the modelled Lorentzian peaks and in red the sum of the modelled lorentzian peaks

area. The main peak around 3595 cm^{-1} and the third peak around 3652 cm^{-1} both show distinct local maxima. The fluid inclusion peak is apparently decoupled from the estimated water content—even if the core of the garnet shows the highest water content and is often associated with a large fluid inclusion peak. Selected deconvoluted spectra of sample TiAnd (see Fig. 4c for location) are presented in Fig. 8. Deconvolution was performed using four Lorentzian peaks with fixed positions at 3563, 3581, 3604 and 3624 cm^{-1} for the spectra from FPA map. The spectra acquired in the core of the sample with ATR objective allowed us to detect a fifth peak—which appears as a shoulder at low wavenumber, around 3540 cm^{-1}. The main doublet is composed of peak 3563 and 3581 cm^{-1}.

Maps of deconvoluted peaks

An automated process was developed which enables to process the entire maps made of tens of thousands spectra. For ServRod, parameter maps were produced and are displayed in Fig. 9. The positions of peak 2 (3595 cm^{-1}) and peak 3 (3652 cm^{-1}) are varying across the map in a systematic manner while this was not observed for peak 1 (map is available in supplementary material S6). Comparing with compositional maps, it appears that the main peak 3592–3599 cm^{-1} is following the calcium content (Fig. 1d). Even if H is in tetrahedral site, Ca can influence the frequency of stretching of the nearby OH bonds, though its direct influence on water incorporation is not obvious. Peak 3 (Fig. 9b) shows

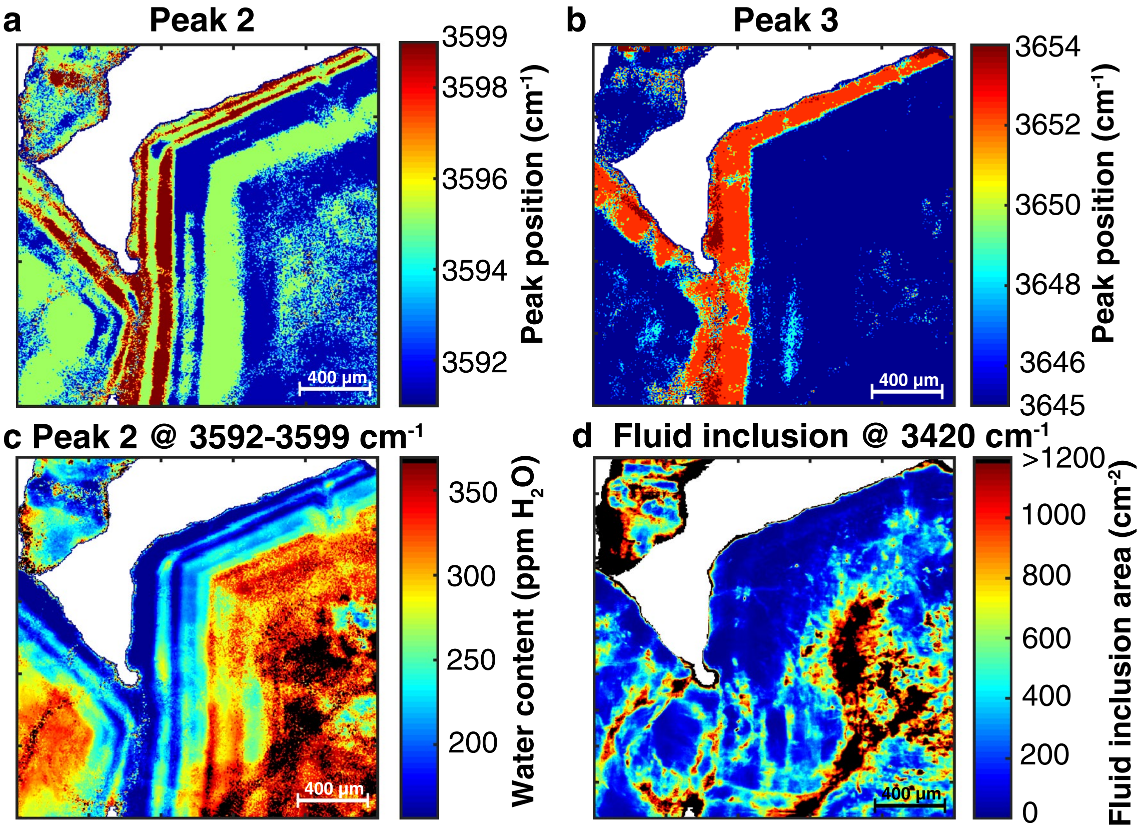

Fig. 9 Maps obtained from the deconvolution of the whole FTIR map of ServRod sample. **a** Local maximum positions of the main peak. **b** Local maximum positions of the third peak. **c** Water map showing the contributions of the main peak to the total water content determined. **d** Fluid inclusion density map expressed as area of the fluid inclusion peak for 1 cm thickness

two main zones with a marked shift of the peak from 3646 in the core to 3654 cm^{-1} at the rim that is not related to any obvious change in garnet composition. Figure 9c represents the main peak area map expressed in ppm H_2O using Eq. 1 (area maps for peak 1 and 3 are shown in supplementary material S7). Figure 9d is a map of the area of the fluid inclusions modelled peak, expressed in cm^{-2} corrected by the thickness of the sample. It does not provide quantitative information about water content in fluid inclusions, as it is an integrated signal through the sample thickness. It only shows a pseudo-density map depending on the localisation of the fluid inclusions across the sample. This map shows that changes in OH band position and intensity are independent of the H_2O band subtraction. The absence of relationship between structural OH and the amount of fluid inclusions containing free H_2O demonstrates that the fluid inclusion correction applied to the FTIR spectra is robust.

Deconvolution maps (location shown in Fig. 4c, d) of a small area of sample TiAnd of the four main peaks observed on FPA spectra were calculated, and compared to X-ray maps of Ti, Fe^{3+} and Al, expected to be cations occupying the octahedral site (Fig. 10 and supplementary material S8). Although the peak positions do not vary significantly across the map, the relative intensities (and area) of each peak are varying. The two major peaks, 3563 cm^{-1} and 3581 cm^{-1} (Fig. 10a, b) are correlated with the Ti content (Fig. 10c) with a 1/1 ratio (Fig. 10d), supporting the hypothesis that Ti is directly influencing water incorporation in point defects related to the OH groups vibrating at these wavenumbers. The peaks 3604 cm^{-1} and 3624 cm^{-1} (Supplementary material S8) appear to be correlated with the Al content, though they contain less than 10% of the total water quantified.

Discussion

Spatial resolution and limitations of the mapping approach

The resolution of the EPMA is dependent on the excitation volume of the electron beam and is typically about 1–2 µm for the mapping conditions used in this study. The maximum resolution of the FTIR is related to the wavelength of infrared light from 3–2.7 µm in the 3300–3700 cm^{-1} absorption region of OH in garnet. The minimum resolution of a single tile in the FPA detector images an area of 2.7 × 2.7 µm. We

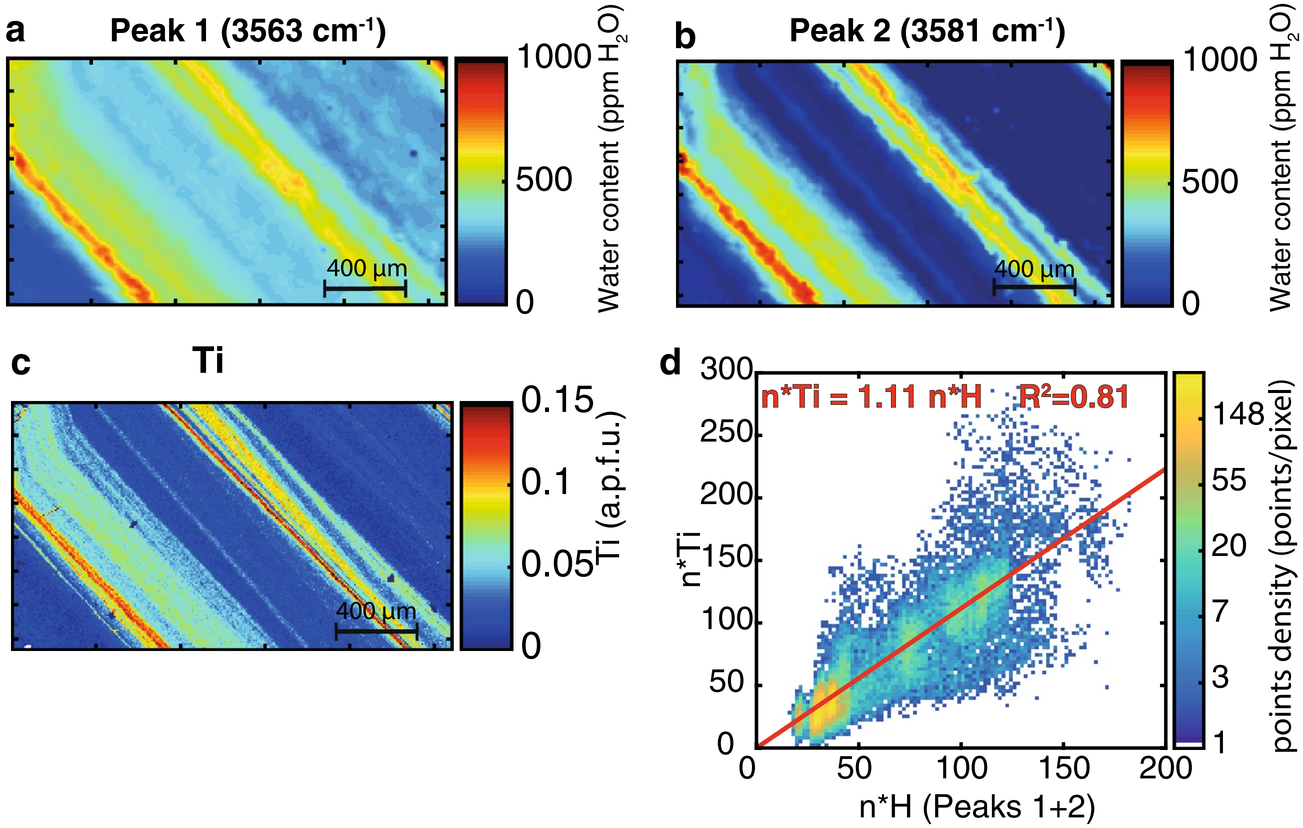

Fig. 10 Maps obtained from the deconvolution of the FTIR map of TiAnd sample with map of cations occupying the octahedral sites determined from the compositional maps, expressed in apfu. Only a small representative zone has been plotted, show in Fig. 4c, d. **a** Water content contributions of the peak at 3563 cm^{-1} (**b**) of the peak at 3581 cm^{-1}. **c** Ti apfu map. **d** Plot showing the number of moles/t of Ti versus the number of moles/t of H for peaks 1 and 2. The plot is a density plot, and only represents a selection of 37,960 analyses (see Fig. 4c, d)

applied a 2 × 2 binning for the ServRod and an 8 × 8 binning for the TiAnd resulting in a maximum resolution of 5.4 and 21.6 µm. The main limitation of the combination of maps presented here is related to the correlation between near-surface analyses (EPMA) and transmission analyses (FTIR). The different zones might be slightly inclined, leading to a smearing out of the signal. We have shown that Ti and H are directly correlated in the ServRod (Fig. 4) and thus the comparison between the EMPA Ti map and the FTIR H_2O map can be used to assess the resolution for this 270-µm-thick sample. The features at the 100-µm scale are all easily resolved and visible on both maps. The smallest features seen in the EPMA map are at the scale of 10 µm and these are not resolved with the FTIR map. However, in the detailed maps (Fig. 6a, b) and deconvoluted peak map of Fig. 9c, features of 30 µm are resolved, in agreement with the study of Jollands et al. (2019). This is further confirmed by the comparison of the Ti map (Fig. 10c) with the map of the 3581 cm^{-1} peak in TiAnd (Fig. 10b, d).

We recommend that the grain diameter should be at least ten times bigger than the thickness of the measured section and that the section is made near its centre. If the grain is too thin compared to the thickness of the rock section, it will produce mixed FTIR spectra, which leads to noise in the FTIR map as seen on the upper left corner of the ServRod sample (Fig. 4). A ten times bigger grain diameter ensures that growth zoning is nearly perpendicular to the surface (considering a rounded approximation as shape of the grain, cut in its centre).

Other issues compromising the FTIR map are mineral or fluid inclusions and cracks. Fluid inclusions can be filtered by spectra deconvolution (Fig. 9d). The effect of mineral inclusion depends on the type of inclusion and on the ratio of the inclusion diameter versus the thickness of the mineral section measured. Usually, the inclusions show an overtone region—or harmonics of Si–O bonds vibrations—in the middle infrared between 1400 and 2200 cm^{-1} specific of the mineral type. As garnet shows characteristic peaks in the overtone range 1600–2000 cm^{-1}, the possible effects of mineral inclusion can be detected. The use of overtone-thickness correction when possible or thresholds on the overtone help to remove the largest inclusions (e.g. Fig. 4c, d). It remains that small inclusions near the surface (Fig. 4d) will not be visible in the water map. By contrast, some inclusions are visible in the water map but not in the EPMA maps—see white zones in Fig. 4c, d. The cracks may cause dispersion of the IR light, and might be partially filled with alteration products or even contaminated by organic products due to the polishing (epoxy, glue, diamond paste solvent). Geometric and oriented features are easily identified as artefacts.

The detection limit of transmission FTIR is linked to the sample thickness. Small grains with very low water contents may not be measurable because of the limited thickness. The opposite is also true, a sample with very high water content cannot be measured by transmission because even thin enough sections would result in complete absorption. This is the case for the core of our TiAnd sample. Considering these constraints, ideal is a grain of 1–3 mm in diameter, prepared in a section of 100–300 µm (a first guess on water content helps to select the appropriate thickness), which enables quantitative mapping in the range 5–3000 ppm H_2O.

Titanium–H_2O relationships: a new hydrous garnet endmember?

Correlation of Ti and H was already observed in grossular-andradite garnet from skarns by Johnson (2003), but profiles were measured with a square beam of 100 × 100 µm for FTIR and 10 µm beam for EPMA. The mapping with a FPA detector enables a pixel size of 20.6 × 20.6 µm (TiAnd) or 5.6 × 5.6 µm (ServRod) resulting in 24–320 times more analyses for the same area. Our new set of algorithms allows the matching of FTIR H_2O maps with EPMA compositional maps pixel by pixel. Therefore, correlations based on a mapping approach are typically based on 10,000–100,000 s of data points, making it possible to have more robust statistics.

A prerequisite for the correlation of Ti with H on a molar basis in garnet is to have a well-constrained calibration of H_2O absorption in andradite garnet. The published extinction coefficients for garnet vary greatly (from 116 to 14,400 $l \cdot mol^{-1} \cdot cm^{-2}$, see Reynes et al. 2018 for details). For the Ti-rich andradite core of TiAnd, independent combustion measurements for the H_2O content are available (Müntener and Hermann 1994). These values are reproduced within error using the extinction coefficient of 14,400 $l \cdot mol^{-1} \cdot cm^{-2}$ determined for grossular from Maldener et al. (2003), indicating that there is no significant difference in the extinction coefficient between grossular and andradite.

ServRod shows a correlation close to 1:1 between $n \times$ Ti and $n \times$ H suggesting that there is one Ti for each H in the crystal structure (Fig. 6). This suggests that $2H^+$ rather than $4H^+$ replace one Si^{4+} in the tetrahedral site. The resulting charge deficiency is then compensated by two Ti^{4+} in an adjacent octahedral site maintaining local charge balance. An alternative substitution would be that $3H^+$ replaces one Si^{4+}, charge balanced by one Ti^{4+} in an octahedral site. This would result in a 1:3 correlation between n^* Ti and n^* H, which is not observed. The sample TiAnd shows three different slopes in terms of n^* Ti vs n^* H (Fig. 6b). For the low titanium content (TiO_2 ranging from 0.1 to 2 wt%), the slope is 1.28. The second domain is characterised by a slope of 1.89 on a range of 1.6–3 wt% TiO_2 demonstrating a relative excess of Ti in comparison of H in the crystal structure. This is caused by extra charge of Ti^{4+} in the crystal structure being partially compensated by divalent cations on the octahedral site (Morimotoite substitution). In the core of the garnet, for $n \times$ H superior to 370 $mol \cdot t^{-1}$, only few data points are available taken with ATR detector. The slope obtained is 1.16 suggesting that a majority of Ti is linked with H, but a small portion of Ti could be also compensated by Morimotoite substitution.

Relationships between Ti and H in garnet have been previously investigated by Armbruster et al. (1998) by single-crystal X-ray refinement through the category of Ti-rich andradites (1–12 wt% Ti)—some being similar to our sample TiAnd in terms of titanium content and water. They observed that the incorporation of the small Ti^{4+} cation in the octahedral site in the garnet structure causes some distortion favouring the incorporation of bigger cations, such as Fe^{3+} or $(4H)^{4+}$ on the tetrahedral site. In their study, the extra charge introduced by Ti^{4+} in the garnet structure was thought to be entirely compensated by Fe^{2+} in the octahedral site (Morimotoite substitution) or Fe^{3+} in tetrahedral site (Schorlomite substitution). Kühberger et al. (1989) proposed that the OH groups are disposed close to the sides of the tetrahedron, allowing big cations like Fe^{3+} or Fe^{2+} to sit together with one or two H in the tetrahedral site in similar Ti-rich garnets. They demonstrated also that the presence of Ti^{4+} introduces extra charge in the crystal and may be compensated by incomplete silicon vacancy mechanism with $3H^+$ instead of 4 in the tetrahedral site. Our study is the first to provide quantitative evidence that only two H occupy the Si site resulting in a new garnet theoretical hydrous garnet endmember with the formula $Ca_3Ti_2H_2Si_2O_{12}$ (Table 1).

Recalculation of ferrous and ferric iron in garnet

The garnet TiAnd has a very high TiO_2 up to 11 wt%, providing a challenge for correct normalisation due to the large amount of extra charge induced by up 0.7 apfu of Ti. Combining EPMA analysis, X-ray refinements, Mössbauer spectroscopy and bulk water measurements, Müntener and Hermann (1994) were not able to provide charge balanced garnet structural formula. Therefore, they proposed that up to half of the Ti present in the Ti-andradite is present as Ti^{3+} to compensate the charge surplus. However, XANES spectroscopy on these garnets subsequently showed no evidence for any Ti^{3+} (Berry et al. 2007). Our new data provide an elegant solution to this problem. If H_2O incorporation occurs as $(2H)^{2+}$ in the tetrahedral site, then twice more tetrahedral sites are occupied and charge balance is easily attained. Thus $(2H)^{2+}$ vs $(4H)^{4+}$ on the tetrahedral site has also consequences for the recalculation of Fe^{2+}/Fe^{3+} ratio in garnet.

Implications for H_2O retention in garnet

The ServRod sample shows a water content of 200–850 ppm H_2O (Fig. 2a) with multiple zoning preserved during high pressure metamorphism, estimated at 550 ± 60 °C and 2.1 ± 0.3 GPa (Martin et al. 2008). The highest water content is observed in the core of the garnet. Considering the growth of garnet during a typical high pressure–low temperature path during subduction, the core of the garnet has to be growing during prograde metamorphism (e.g. Baxter and Caddick (2013)). Most of the water incorporated as OH groups in the crystal structure was then incorporated during the first stage of the garnet growth and kept during the whole metamorphic cycle. Even the later growth zones are still at 200 ppm H_2O, indicating that during the whole growth of the garnet, OH groups were incorporated.

The oscillatory water zonings correlate with the Ti content, and both appear unaffected by diffusion. Experimental studies on H diffusion in grossular garnet have shown that H potentially diffuses very fast via a proton–polaron mechanism where the loss of a H is compensated by the oxidation of a Fe^{2+} to a Fe^{3+} (Kurka et al. 2005; Reynes et al. 2018). Based on these results, a total loss of H in a garnet grain of 2000 μm diameter would take less than 320 years at the given peak temperature considering this fast oxidation-related mechanism (Supplementary material S9). As the Alpine subduction rates are in the order of 1–2 cm $year^{-1}$ (Handy et al. 2010) a temperature above 500 °C was maintained for several million years. Hydrogen is obviously much more retentive than expected. Higher retentivity could be explained by very low oxygen fugacity at the eclogitic stage slowing down the diffusion of hydrogen. Alternatively, because the H is bound by a coupled substitution with Ti, this might lead to a higher retentivity. This example demonstrates that to apply experimental H diffusivities in garnet to constrain metamorphic timescales it is important to make sure that the same diffusion mechanism is considered.

A final question is whether the measured H_2O represents the total water incorporated during the growth of the garnet or whether some H_2O was lost post formation. The measured OH groups in ServRod garnets are related to only one stable point defect (Ti_2H_2). H in less stable point defects might have been lost near the peak conditions or upon exhumation and cooling. It can be argued that the OH region in the spectrum of the sample ServRod is very simple with only three peaks, when spectra up to eight different peaks have been commonly identified in grossular grown in hydrothermal conditions (Rossman and Aines 1991).

Conclusions

The combination of quantitative compositional maps obtained by EPMA and H_2O maps acquired by FTIR provides constraints on the substitution mechanisms in garnet based on 10,000 to 100,000 data points. FTIR data also provide critical constraints on the environment of the OH groups in the crystal structure. A deconvolution algorithm has been designed to provide maps of single peaks that then can be compared to major and minor element zoning. This new approach has been applied to a grossular-rich garnet from a high-pressure metarodingite and a Ti-rich andradite formed during greenschist facies conditions. In both garnets, two H in the tetrahedral site are charge balanced by two Ti on the octahedral site, resulting in a new hydrous garnet endmember with the formula $Ca_3Ti_2H_2Si_2O_{12}$. Therefore, twice as many Si-vacancies are produced for the same amount of H_2O compared to the classical hydro-grossular defect where four hydrogens occupy a tetrahedral site, with unknown effects on the rheological behaviour of garnet. Our findings impact also on the recalculation of Fe^{2+}/Fe^{3+} in hydrous garnet as the sum of cation is different when only two hydrogens are allocated to a tetrahedral site. The preservation of fine-scale H_2O zoning at the 50 μm scale in the high-pressure garnet provides evidence for minimal diffusional resetting during the burial and exhumation of subducted oceanic crust, indicating that the coupled Ti–H substitution is more retentive than other H defects in garnets that have been previously investigated in experimental diffusion studies.

Acknowledgements We are grateful to G. Bromiley and an anonymous reviewer for their careful reviews, which helped us to improve the presentation of the manuscript, and H. Keppler for editorial handling. This work was financially supported by the Swiss National Science Foundation Grant no. 200021_169062 to J.H. and J.R.

References

Aines R, Rossman G (1984) The hydrous component in garnets: pyralspites. Am Mineral 69:1116–1126

Amthauer G, Rossman G (1998) The hydrous component in garnets: pyralspites. Am Mineral 83:835–840

Andrut M, Wildner M, Beran A (2002) The crystal chemistry of birefringent natural uvarovites. Part IV. OH defect incorporation mechanisms in non-cubic garnets derived from polarized IR spectroscopy. Eur J Mineral 14:1019–1026

Armbruster T, Birrer J, Libowitzky E, Beran A (1998) Crystal chemistry of Ti–bearing andradites. Eur J Mineral 10:907–921

Arredondo EH, Rossman GR, Lumpkin GR (2001) Hydrogen in spessartine–almandine garnets as a tracer of granitic pegmatite evolution. Am Mineral 86:485–490

Basso R, Cimmino F, Messiga B (1984) Crystal-chemistry of hydrogarnets from 3 different microstructural sites of a basaltic metarodingite from the Voltri-massif (Western Liguria, Italy). Neues Jahrbuch Fur Mineralogie-Abhandlungen 148(3):246–258

Baxter E, Caddick M (2013) Garnet growth as a proxy for progressive subduction zone dehydratation. Geology 41(6):643–646

Berry A, Walker A, Hermann J, O'Neill H, Foran G, Gale J (2007) Titanium substitution mechanisms in forsterite. Chem Geol 242:176–186

Cohen-Addad C, Ducros P, Bertaut EF (1967) Etude de la substitution du groupement SiO_4 par $(OH)_4$ dans les composés $Al_2Ca_3(OH)_{12}$ et $Al_2Ca_3(SiO_4)_{2.16}(OH)_{3.36}$ de type grenat. Acta Crystallogr A 23:220–230

Foreman D (1968) Neutron and X-ray diffraction study of $Ca_3Al_2(O_4D_4)_3$, a garnetoid. J Chem Phys 48:3037–3041

Geiger CA, Langer K, Bell DR, Rossman GR, Winkler B (1991) The hydroxide component in synthetic pyrope. Am Mineral 76:49–59

Geiger CA, Rossman GR (2018) IR spectroscopy and OH– in silicate garnet: the long quest to document the hydrogarnet substitution. Am Mineral 103:384–393

Handy MR, Schmid SM, Bousquet R, Kissling E, Bernoulli D (2010) Reconciling plate-tectonic reconstructions of Alpine Tethys with the geological-geophysical record of spreading and subduction in the Alps. Earth Sci Rev 102:121–158

Johnson EA (2003) Hydrogen in nominally anhydrous crustal minerals. Dissertation, California Institute of Technology

Jollands M, Kempf E, Hermann J, Müntener O (2019) Coupled inter-site reaction and diffusion: rapid dehydrogenation of silicon vacancies in natural olivine. Geochim Cosmochim Acta 262:220–242

Khomenko VM, Langer K, Beran A, Koch-Müller M, Fehr T (1994) Titanium substitution and OH-bearing defects in hydrothermally grown pyrope crystals. Phys Chem Miner 20:483–488

Kühberger A, Fehr T, Huckenholz HG, Amthauer G (1989) Crystal chemistry of a natural schorlomite and Ti–andradites synthetized at different oxygen fugacities. Phys Chem Miner 16:734–740

Kurka A, Blanchard M, Ingrin J (2005) Kinetics of hydrogen extraction and deuteration in grossular. Mineral Mag 69(3):359–371

Lager GA, Armbruster T, Faber J (1987) Neutron and X-ray diffraction study of hydrogarnet $Ca_3Al_2(O_4H_4)_3$. Am Mineral 72:756–765

Lanari P, Vidal O, De Andrade V, Dubacq B, Lewin E, Grosch E, Schwartz S (2014) XMapTools: a MATLAB-based program for electron microprobe X-ray image processing and geothermobarometry. Comput Geosci 62:227–240

Lanari P, Vho, A. Bovay T, Airaghi L, Centrella S (2019) Quantitative compositional mapping of mineral phases by electron probe micro-analyser. In: Ferrero S, Goncalves P, Grosch E (ed) Metamorphic geology: microscale to mountain belts, vol 478. Geological Society of London, Special Publications, London

Lu R, Keppler H (1997) Water solubility in pyrope to 100 kbar. Contrib Mineral Petrol 129:35–42

Maldener J, Hösch A, Langer K, Rauch F (2003) Hydrogen in some natural garnets studied by nuclear reaction analysis and vibrational spectroscopy. Phys Chem Miner 30:337–344

Martin S, Rebay G, Kienast J-R, Mével C (2008) An eclogitised oceanic palaeo-hydrothermal field from the St. Marcel Valley (Italian Western Alps). Ofioliti 33(1):49–63

Müntener O, Hermann J (1994) Titanian andradite in a metapyroxenite layer from the Malenco ultramafics (italy): implications for Ti-mobility and low oxygen fugacity. Contrib Mineral Petrol 116:156–168

O'Haver T (2015) A Pragmatic* Introduction to Signal Processing with applications in scientific measurement; an illustrated essay with free software and spreadsheet templates to download. https://terpconnect.umd.edu/~toh/spectrum/. Accessed 14 July 2018

Reynes J, Jollands MC, Hermann J, Ireland T (2018) Experimental constraints on hydrogen diffusion in garnet. Contrib Mineral Petrol 173(69):68–70

Rossman GR, Aines RD (1991) The hydrous components in garnets: grossular-hydrogrossular. Am Mineral 76:1153–1164

Tartarotti P, Martin S, Monopoli B, Benciolini L, Schiavo A, Campana R, Vigni I (2017) Geology of the Saint-Marcel valley metaophiolites (Northwestern Alps, Italy). J Maps 13(2):707–717